Spectroscopy of cesium Rydberg atoms in strong radio-frequency fields

Yuechun Jiao,[1,2] Xiaoxuan Han,[1,2] Zhiwei Yang,[1,2] Jingkui Li,[1,2] Georg Raithel,[1,3] Jianming Zhao,[1,2,*] and Suotang Jia[1,2]

[1]*State Key Laboratory of Quantum Optics and Quantum Optics Devices, Institute of Laser Spectroscopy, Shanxi University, Taiyuan 030006, China*

[2]*Collaborative Innovation Center of Extreme Optics, Shanxi University, Taiyuan 030006, China*

[3]*Department of Physics, University of Michigan, Ann Arbor, Michigan 48109-1120, USA*

(Received 5 January 2016; published 17 August 2016)

We study Rydberg atoms modulated by strong radio-frequency (rf) fields with a frequency of 70 MHz. The Rydberg atoms are prepared in a room-temperature cesium cell, and their level structure is probed using electromagnetically induced transparency (EIT). As the rf field increases from the weak- into the strong-field regime, the range of observed rf-induced phenomena progresses from ac level shifts through increasingly pronounced and numerous rf modulation sidebands to complex state mixing and level crossings with high$-l$ hydrogenlike states. Weak anharmonic admixtures in the rf field generate clearly visible modifications in the Rydberg EIT spectra. A Floquet analysis is employed to model the Rydberg spectra, and good agreement with the experimental observations is found. Our results show that all-optical spectroscopy of Rydberg atoms in vapor cells can serve as an antenna-free, atom-based, and calibration-free technique to measure rf electric fields and to analyze their higher-harmonic contents.

DOI: 10.1103/PhysRevA.94.023832

I. INTRODUCTION

Atom-based field measurement has made significant progress in reproducibility, accuracy, and resolution. Atoms have been successfully used for magnetometry with high sensitivity and spatial resolution [1,2]. Rydberg atoms (highly excited atoms with principal quantum numbers $n \gg 1$) have applications in electrometry due to their large dc polarizabilities and microwave-transition dipole moments, which follow respective scaling laws $\propto n^7$ and $\propto n^4$ [3] and make these atoms extremely sensitive to dc and ac electric fields. Rydberg electromagnetically induced transparency (EIT) [4] in atomic vapor cells has been used to realize a giant dc Kerr coefficient [5] and to measure the electric fields of electromagnetic radiation with a large dynamic range [6]. Radio-frequency (rf)-dressed Rydberg EIT has been demonstrated in a number of applications, including measurements of microwave fields and polarizations [7–9], millimeter waves [10], static electric fields [11], and precise determinations of quantum defects [12]. The rf measurement via Rydberg EIT in a vapor cell does not require vacuum or atomic-beam and laser-cooling infrastructure; it offers significant potential for miniaturization [13], and it covers a frequency range extending from the megahertz into the terahertz range. The method is also suitable to perform subwavelength imaging of microwave electric-field distributions [14,15] and to study inhomogeneities of such fields [16].

Microwave fields have been measured and mapped by resonantly driving Rabi oscillations between ground-state hyperfine (magnetic dipole) states at the ^{87}Rb hyperfine frequency [17–20]. These works were performed in vapor cells placed within the microwave field. There also is a large body of work on microwave spectroscopy of Rydberg atoms (see [3] and references therein).

Due to the invariable nature of the atomic response of Rydberg EIT spectra to an applied rf field, Rydberg EIT spectroscopy represents an atom-based, calibration-free field-measurement method. This differs from traditional rf-field measurement, where antenna structures are employed that can be bulky and require periodic calibration. The implementation of Rydberg EIT spectroscopy as a measurement method requires a theoretical model of the experimentally produced spectra. In the weak-field regime, field measurement in the radio FM band (tens to hundreds of megahertz) using Rydberg EIT has been modeled well by perturbation theory [21]. In strong rf fields, the Rydberg levels exhibit higher-order couplings and state mixing with high$-l$ hydrogenlike states (states with quantum defects $\ll 1$). In this case, many atomic levels become coupled, and the atom-field interaction can no longer be modeled using perturbation theory. Typically, the rf field to be probed is periodic over the time scale of interest. Then, Floquet theory [22,23], a nonperturbative method akin to band-structure theory, can be used to accurately describe the system.

In this work, we present EIT spectroscopy of Rydberg atoms modulated by strong rf fields with a frequency of 70 MHz. The dependence of the Rydberg spectrum on the strength of the rf field is investigated for harmonic and slightly distorted rf signals. The Rydberg spectra exhibit rf-field-induced level shifts, rf sidebands, and, in the strong-rf-field regime, state mixing with high$-l$ hydrogenlike states. We use the Floquet treatment to model the Rydberg-level shifts, state mixing, and excitation rates. The rf field is deduced by comparing experimental and calculated Floquet maps. We also find that the Rydberg spectrum exhibits different sideband structures for slightly distorted rf wave forms, demonstrating that the atomic response is sensitive to the small anharmonic content of the applied rf signal.

II. EXPERIMENTAL SETUP

A schematic of the experimental setup is shown in Fig. 1(b). The experiments are performed in a room-temperature cesium cell. The relevant atomic levels form a three-level system,

*Corresponding author: zhaojm@sxu.edu.cn

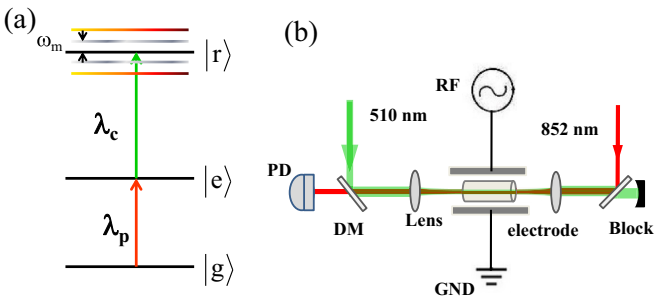

FIG. 1. (a) Energy-level scheme of Rydberg EIT. The probe laser λ_p is resonant with the transition $|g\rangle \rightarrow |e\rangle$, and the coupling laser λ_c is scanned through resonances from $|e\rangle$ into Rydberg states $|r\rangle$. An applied rf electric field (frequency $\omega_m = 2\pi \times 70$ MHz) produces field-mixed Rydberg levels with rf modulation sidebands, which are separated in energy by even multiples of $\hbar\omega_m$. (b) Schematic of the experimental setup. The coupling and probe lasers counterpropagate through a cesium vapor cell. The probe beam is passed through a dichroic mirror (DM) and is detected with a photodiode (PD). The probe transmission through the cell is measured as a function of coupler frequency.

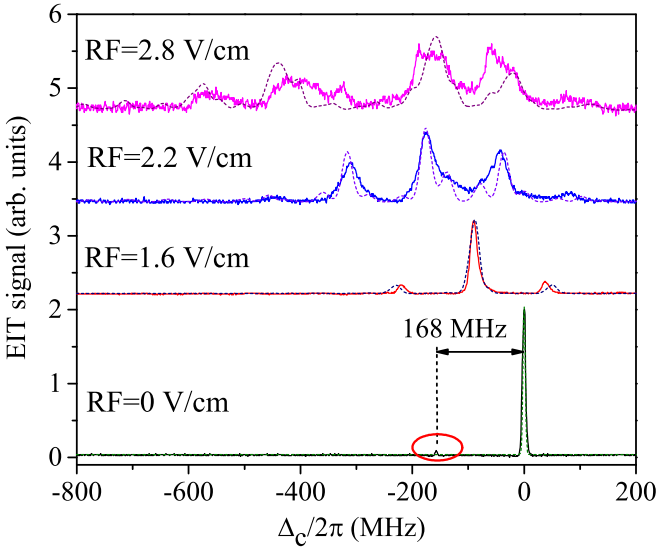

FIG. 2. Bottom curve: Rydberg EIT spectrum without rf field for the $57S_{1/2}$ Rydberg state. The dominant peak at zero detuning corresponds to the double resonance $6S_{1/2}$ $(F = 4) \rightarrow 6P_{3/2}$ $(F' = 5) \rightarrow 57S_{1/2}$, while the small peak at -168 MHz results from the $6S_{1/2}$ $(F = 4) \rightarrow 6P_{3/2}$ $(F' = 4) \rightarrow 57S_{1/2}$ resonance. Top curves: measurements (solid lines) and calculations (dashed lines) of Rydberg EIT spectra with harmonic rf level modulation (modulation frequency $\omega_m = 2\pi \times 70$ MHz) and the indicated rf-field amplitudes. The main EIT peak is ac Stark shifted and develops two to four even-harmonic sidebands. The broadening of the peaks at 2.2 and 2.8 V/cm amplitude is due to complex rf-induced coupling of the $57S_{1/2}$ level with hydrogenlike Rydberg levels (states with quantum defects $\ll 1$) and possibly due to Rydberg-atom interactions (see Sec. V).

illustrated in Fig. 1(a), consisting of the ground state $6S_{1/2}$ $(F = 4)$, denoted $|g\rangle$; the intermediate state $6P_{3/2}$ $(F' = 5)$, denoted $|e\rangle$; and the $57S_{1/2}$ Rydberg state. A weak probe laser (wavelength $\lambda_p = 852$ nm, Rabi frequency $\Omega_p = 2\pi \times 7.4$ MHz, power of 1.5 μW, and $1/e^2$ waist $w_0 = 75$ μm) is resonant with the transition $|g\rangle \rightarrow |e\rangle$, while a strong coupling laser ($\lambda_c = 510$ nm, Rabi frequency $\Omega_c = 2\pi \times 7.2$ MHz, power of 45 mW, and $1/e^2$ waist $w_0 = 95$ μm) scans through the $|e\rangle \rightarrow |r\rangle$ Rydberg transitions, where $|r\rangle$ is the $57S_{1/2}$ Rydberg level or an rf-dressed or rf-coupled Rydberg level close to it. The counterpropagating coupler and probe beams are linearly polarized, with polarizations parallel to each other. The coupling laser induces an increased transmission for the probe laser when an EIT double-resonance condition is met. The EIT signal is observed by measuring the transmitted power of the probe beam.

The Rydberg level is modulated with a rf electric field with modulation frequency $\omega_m = 2\pi \times 70$ MHz and variable field strength. The rf field, provided by a function generator (Agilent 33250 A), is applied to parallel-plate electrodes [spacing of 27.0 mm; see Fig. 1(b)]. The electric field between the two electrodes is uniform along the entire length of the atom-field interaction volume and parallel to the polarizations of the laser beams. At low rf fields, the modulation generates an overall ac shift, because S Rydberg levels of cesium exhibit a quadratic Stark effect, as well as a sequence of modulation sidebands [21], as sketched in Fig. 1(a). In the strong-field domain, complex Rydberg EIT spectra arise from strongly mixed Floquet states and their rf sidebands.

An extra pair of coupler and probe laser beams that are equivalent to the ones used in the rf spectroscopic cell are counterpropagated through an auxiliary EIT setup with an electric-field-free cell (not shown in Fig. 1). The EIT signal from the auxiliary setup defines the zero-detuning frequency reference point for all spectra we show. The black line at the bottom of Fig. 2 presents the EIT spectrum without rf field, where the probe laser is locked to the $|g\rangle \rightarrow |e\rangle$ transition, while the coupling laser is scanned across the $|e\rangle \rightarrow |57S_{1/2}\rangle$ transition. The main peak in the reference spectrum defines the position of zero detuning. The small peak red detuned by 168 MHz from the main peak, marked with a red circle, is the EIT signal due to the hyperfine component $F' = 4$ of the intermediate $6P_{3/2}$ level, which is 251 MHz below the $F' = 5$ component. (Note that a Doppler factor of $\lambda_p/\lambda_c - 1 = 0.67$ applies, due to which the observed hyperfine interval becomes 0.67×251 MHz $= 168$ MHz.)

III. RYDBERG EIT MEASUREMENTS IN STRONG rf FIELDS

The top three curves in Fig. 2 show Rydberg EIT sideband spectra with an applied sinusoidal rf signal with $\omega_m = 2\pi \times 70$ MHz and amplitudes $F = 1.6$ V/cm and $F = 2.2$ and 2.8 V/cm, as well as the corresponding calculations. It is clearly seen that in weak fields the main EIT peak (central band) is redshifted due to the cycle-averaged ac Stark effect. Since the rf frequency is much smaller than the characteristic atomic frequency (the Kepler frequency is $\approx$40 GHz for the given state), the ac shift follows from the dc polarizability $\alpha/h = 137$ MHz/(V/cm)^2 for $57S_{1/2}$. For amplitudes $F = 1.6$ and 2.2 V/cm the expected ac shifts of the central band, $-\alpha F^2/4$ [21], approximately equal -88 and -166 MHz, respectively. These estimates are in good agreement with the spectra for fields of 1.6 and 2.2 V/cm

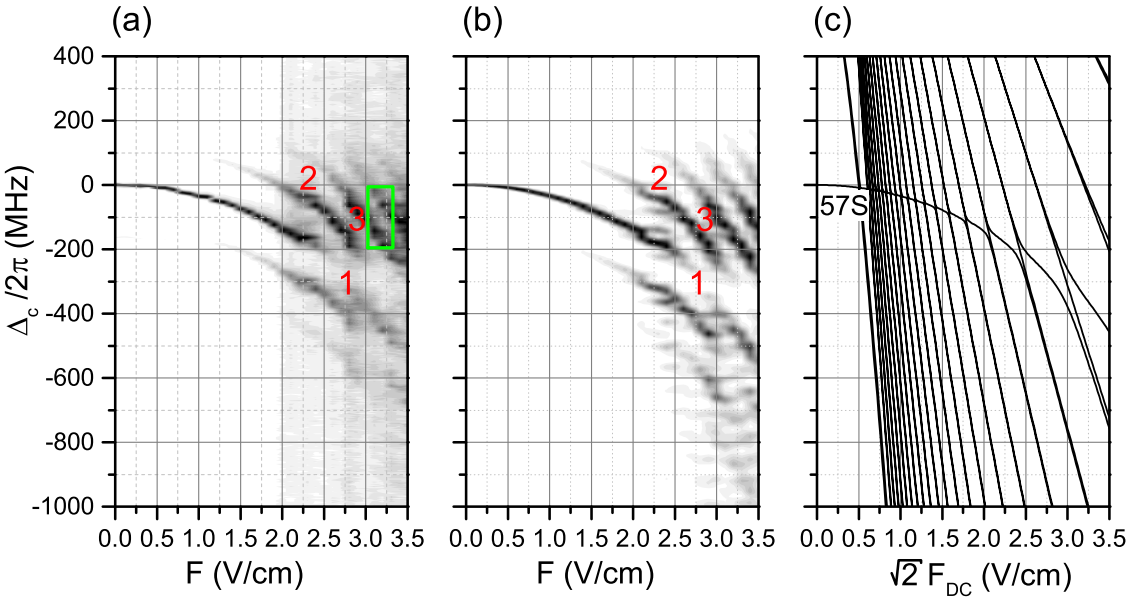

FIG. 3. (a) Measurement and (b) calculation of Rydberg excitation spectra as a function of rf electric-field amplitude F. The sinusoidal rf field modulates the Rydberg levels with a modulation frequency $\omega_m = 2\pi \times 70$ MHz. Labels 1–3 indicate spectral features discussed in the text. In (b), we convolute the calculated relative excitation rates with a two-dimensional line broadening function, explained in Sec. V. For comparison, (c) shows a Stark map in a dc electric field on a field axis scaled such that the rms fields in (a)–(c) match. The map shows the quadratic Stark effect of the $57S_{1/2}$ level [polarizability $\alpha/h = 137$ MHz/(V/cm)^2], a fan of hydrogenic states that exhibit linear Stark effect, and the mixing between these states.

in Fig. 2. The second-harmonic sidebands, which have band indices $N = \pm 2$, are separated by ± 140 MHz from the $N = 0$ band. In the limit of small F, the relative strengths of the $N = \pm 2$ bands, normalized by the strength of the central band, are given by $|J_1(y)/J_0(y)|^2$, where $y = \alpha F^2/(8\hbar\omega_m)$ [21] and $J_i(y)$ is the ith Bessel function of the first kind. The Bessel-function expression allows one to calculate the relative strengths of the sidebands in the weak-field limit. For $F = 1.6$ and 2.2 V/cm one expects relative strengths of 0.11 and 0.52, respectively, in good qualitative agreement with Fig. 2. For the case $F = 2.2$ V/cm, the line profiles of all bands, including the weak $N = \pm 4$ bands, are already significantly broadened by the rf-induced mixing of the $57S_{1/2}$ state with the manifold of hydrogenlike states for $n = 53$. As we increase the rf field further, the zero-order ($N = 0$) band drops out at fields for which $J_0(y) \approx 0$; also, the signals generally become weaker because of the strong mixing of the $57S_{1/2}$ state with the manifold of hydrogenlike states (for more details see Fig. 3). For comparison, in Fig. 2 we also show calculated spectra (dashed lines); in the calculation we use Floquet theory and a line-broadening model, as discussed in detail in Secs. IV and V.

We have performed a series of measurements such as in Fig. 2, in which we have increased the amplitude of the sinusoidal rf modulation field from 0 to 3.5 V/cm in steps of 0.1 V/cm. In Fig. 3(a), the spectrum is seen to progress through several regimes that show how the oscillator strength of the $|e\rangle \rightarrow |r\rangle$ Rydberg transition becomes spread over the rf modulation sidebands of the $57S_{1/2}$ level as well as other Rydberg states and their rf sidebands that the $57S_{1/2}$ level couples with. In the weak-field regime ($F < 0.7$ V/cm), the $N = 0$ band is the only one clearly visible, and it exhibits the aforementioned cycle-averaged quadratic ac Stark shift. In an intermediate regime (0.7 V/cm $\lesssim F \lesssim$ 2.5 V/cm) the even modulation orders $N = \pm 2$ and ± 4 rise in strength, while the $N = 0$ order decreases in strength and drops out at about $F_A = 2.7$ V/cm (label 1 in Fig. 3). In the weak-field model [21], the dropout would occur at the field for which $J_0(y) = 0$, corresponding to $y = 2.40$ and a field of about $F_B = 3.1$ V/cm in the present case. The deviation between F_A and F_B reflects the fact that at $\sim$3 V/cm the $57S_{1/2}$ level is already deeply within the manifold of hydrogenlike states [see Fig. 3(c)], and the weak-field model does not apply any more. Inspecting Figs. 3(b) and 3(c), it is seen that the rf-induced coupling with hydrogenic states pushes the $N = 0$ band of the $57S_{1/2}$ level to an energy below the corresponding $57S_{1/2}$ line in the dc field. This effect amounts to an increase of the polarizability α, which explains why the $N = 0$ dropout occurs at a field F_A that is lower than the weak-field estimate F_B.

In the strong-field regime ($F \gtrsim 2.5$ V/cm), the shifts of the rf-induced sidebands as a function of field turn from quadratic into linear (label 3 in Fig. 3), indicating the strong rf-induced mixing of the $57S_{1/2}$ level with rf-induced superpositions of hydrogenic states that exhibit linear Stark shifts. The undulations of the spectrum, observed below label 2 in Fig. 3, are a manifestation of the complex rf-induced coupling behavior of the $57S_{1/2}$ level with the large number of such hydrogenic states.

The absence of odd rf modulation sidebands in Fig. 3 indicates the absence of dc bias fields. In principle, dc fields could originate from stray charges on the cell walls or from external electric fields penetrating from outside the cell into the probe region. However, dc fields appear to be shielded (see [4] and Fig. 7 below).

IV. FLOQUET MODEL

For a quantitative interpretation of our measured spectra, we use a nonperturbative Floquet method, the accuracy of which is only limited by the size of the atomic basis set used. The method has previously been described in Refs. [24,25]. Here, we provide the most relevant results.

The coupling-laser frequencies $\omega_{\nu,N}$ at which EIT resonances are observed and their relative excitation rates $S_{\nu,N}$ are given by

$$\hbar\omega_{\nu,N} = W_\nu + N\hbar\omega_m,$$
$$S_{\nu,N} = (eF_L/\hbar)^2 \left| \sum_k \tilde{C}_{\nu,k,N}\, \hat{\epsilon} \cdot \langle k|\hat{\mathbf{r}}|6P_{3/2},m_j\rangle \right|^2, \quad (1)$$

with the coupling-laser electric-field amplitude F_L and polarization vector $\hat{\epsilon}$. The $\langle k|\hat{\mathbf{r}}|6P_{3/2},m_j\rangle$ are the electric dipole matrix elements of the Rydberg basis states $|k\rangle = |n,\ell,j,m_j\rangle$ with $|6P_{3/2},m_j\rangle$. The Floquet energies W_ν follow from the eigenphases of the time-evolution operator $\hat{U}(T)$ integrated through one period of the rf field, $T = 2\pi/\omega_m$. The Floquet levels W_ν have rf-dressed sidebands that are associated with the exchange of N rf photons during the excitation. The Fourier coefficients $\tilde{C}_{\nu,k,N}$ are obtained from the time-dependent Floquet wave packets $|\Psi_\nu(t)\rangle$ and exact time-periodic functions $C_{\nu,k}(t)$ according to

$$|\Psi_\nu(t)\rangle = e^{-iW_\nu t/\hbar} \sum_k C_{\nu,k}(t)|k\rangle$$
$$= e^{-iW_\nu t/\hbar} \sum_k \sum_{N=-\infty}^{\infty} \tilde{C}_{\nu,k,N} e^{-iN\omega_m t}|k\rangle,$$
$$\tilde{C}_{\nu,k,N} = \frac{1}{T}\int_0^T C_{\nu,k}(t) e^{iN\omega_m t} dt. \quad (2)$$

The theory is similar to methods described elsewhere [22,23]. In our implementation, the time-evolution operator $\hat{U}(T)$ is determined via direct integration of the Schrödinger equation through one cycle. The required electric dipole matrix elements between the basis states are computed as explained in [26]. In the next step, all Floquet energies W_ν and the corresponding Floquet wave packets at the beginning of the cycle, $|\Psi_\nu(t=0)\rangle$, are found. This is the most time-consuming step. Using $|\Psi_\nu(t=0)\rangle$ as initial conditions, all Floquet wave packets $|\Psi_\nu(t)\rangle$ are subsequently computed over one cycle, $0 < t < T$. This step requires a second integration of the Schrödinger equation through one cycle. During the course of the second integration, the Fourier coefficients of the Floquet wave packets $\tilde{C}_{\nu,k,N}$ are determined according to Eq. (2). Finally, the Fourier coefficients and the (known) electric dipole matrix elements $\langle k|\hat{\mathbf{r}}|6P_{3/2},m_j\rangle$ yield the relative excitation rates according to Eq. (1). For more details, see [25].

The basis $\{|k\rangle\}$ must be chosen to be large enough to cover important couplings. Since the theory has to accurately describe mixing with hydrogenic states, it is obvious that the basis has to include all ℓ and j values, which are $\ell = 0,\ldots,n-1$ and $j = \ell \pm 1/2$, respectively (for $\ell = 0$, $j = 1/2$). Since the fields are π polarized, $m_j = 1/2$. We have performed calculations with basis sets with principal quantum numbers $51.1 < n_{\rm eff} < 54.9$ (319 atomic basis states) and with $52.05 < n_{\rm eff} < 53.95$ (109 atomic basis states). A comparison of the results shows that, at our current level of precision, the small basis set is large enough to describe the experimental results. In our method, the time-evolution operator $\hat{U}(T)$ is integrated in time steps Δt through one rf cycle. The value of Δt must be small enough that $|W_k - W_{k'}|\Delta t/\hbar \leqslant 2\pi$ for all energy differences $W_k - W_{k'}$ for basis states $|k\rangle$ and $|k'\rangle$. In the present case, $\Delta t = T/2048$ to $T/4192$ is appropriate.

For the number of rf photons N that may be exchanged during the optical excitation process, we use a range $-20 \leqslant N \leqslant 20$, which, for the given rf frequency, is sufficiently large to cover the energy range of the experimental data shown in Figs. 2 and 3 (and also Figs. 6 and 7 below). Hence, a number of $109 \times 41 = 4469$ dressed atom-field states is sufficient to describe our experimental work.

V. LINE-BROADENING MODEL AND DATA INTERPRETATION

In comparing the experimental and calculated spectra, the experimental electric-field axis has been scaled such that the spectra show best agreement. In addition, to include EIT line broadening in our model, we convolute the relative excitation rates $S_{\nu,N}$ with a two-dimensional empirical line-broadening function that accounts for rf electric-field inhomogeneity, laser linewidths, EIT saturation broadening, and additional line broadening at high rf fields. At the current level of precision, it is sufficient to use a broadening function that factorizes into a product of Gaussians, $G_\nu(\Delta\nu) \times G_F(\Delta F)$.

The FWHMs of the Gaussians $G_\nu(\Delta\nu)$ and $G_F(\Delta F)$ are adjusted to achieve reasonable agreement between experimental and calculated spectra. For the data in Fig. 3(b), we employ a $G_F(\Delta F)$ with a FWHM of 4% of the average field, which amounts to 0.15 V/cm at the high-field limit in Fig. 3. This degree of electric-field broadening is in line with rf electric-field inhomogeneities one may expect along the length of the atom-field interaction region in the spectroscopic cell. Further, to achieve satisfactory agreement between experimental and calculated spectra, we use Gaussians $G_\nu(\Delta\nu)$ whose FWHM linearly increases from 5 MHz at $F = 0$ to 20 MHz at $F = 2.2$V/cm and remains constant at 20 MHz at larger fields. We attribute the apparent increase in excitation bandwidth at higher fields to the increase in the ac dipole moment of the excited Floquet Rydberg levels between 0 and ~2.2 V/cm (the ac dipole moments are given by the negative slopes of the bands in Fig. 3). Larger dipole moments may cause larger interactions between Rydberg atoms in the cell, which could lead the apparent increase in excitation bandwidth. Verification of this hypothesis will require future investigation.

The agreement between experimental and calculated rf EIT spectra, seen in Fig. 3, is very good, in terms of both the positions of spectral features and relative signal strengths. From the static-field Stark map in Fig. 3(c) it is evident that the $57S_{1/2}$ level first intersects with hydrogenlike states at fields of about 0.6 V/cm. The widths of the avoided crossings between the levels further indicate that substantial mixing between the $57S_{1/2}$ level and the hydrogenlike states begins at rf fields of about 2 V/cm. Accordingly, the rf-field data in Figs. 3(a) and 3(b) exhibit a transition from a plain sideband-modulation structure into a more complex spectrum beginning at a field

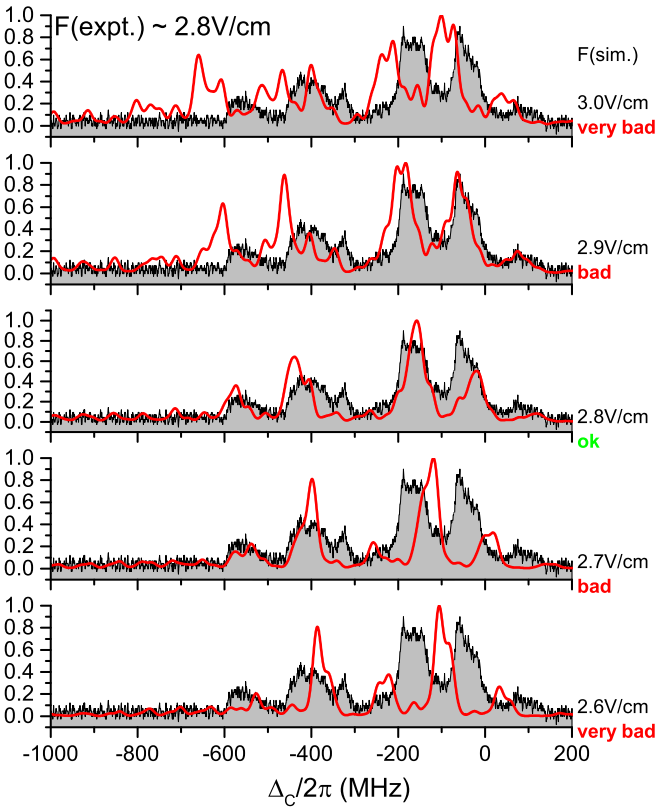

FIG. 4. Comparison between the experimental rf spectrum at $F = 2.8$ V/cm from Fig. 2 (gray shaded curve) with spectra calculated for electric-field values indicated on the right (red lines). Only the calculated curve for $F = 2.8$ V/cm agrees reasonably well with the measurement. Therefore the rf field is deduced to be 2.8 V/cm, with an uncertainty better than ± 0.1 V/cm.

of about 2 V/cm. Comparing Figs. 3(a) and 3(b) we note agreement even in fine details, such as the significant kink of the $N = 2$ band at 2.3 V/cm (just below label 2) and the groups of levels that form bridges between the $N = 0$ and $N = -2$ bands at 3.0 V/cm (to the lower right of label 1). In the high-field regime, most of the spectral features are not due to single, isolated levels (Floquet states and rf sidebands) but are due to signals associated with several levels merging into compound structures (also see Fig. 5 below). The beading within the steep bands in the experimental data reflects the 0.1 V/cm step size in the electric-field change between the scans, which is the same in experiment and calculation.

Comparing calculated with experimental Floquet spectra, we estimate the calibration uncertainty between the experimental and theoretical electric-field axes to $\approx 3\%$ (peak to peak), corresponding to ≈ 0.1 V/cm at 3.5 V/cm. The uncertainty of the rf electric-field calibration is primarily based on the fact that we find a good match between experimental and calculated data only over a range of about 3% of the electric-field calibration factor. The procedure used to match experimental with simulated spectra is illustrated in Fig. 4 for the case $F = 2.8$ V/cm (top curve in Fig. 2 and gray shaded spectra in Fig. 4). In Fig. 4, the experimental spectrum is compared with a series of simulated spectra. The figure clearly shows that the simulated spectrum for $F = 2.8$ V/cm presents the best match. A deviation of ± 0.2 V/cm from the value 2.8 V/cm leads to a dramatic mismatch between experiment and simulation. A deviation of ± 0.1 V/cm leads to a less dramatic but still significant discrepancy between experiment and simulation. Hence the rf field is determined to be $F = 2.8$ V/cm, with an uncertainty better than ± 0.1 V/cm. Implementation of the matching procedure for the entire array of spectra shown in Fig. 3 leads to an rf electric-field calibration with a peak-to-peak uncertainty of $\approx 3\%$.

The described procedure amounts to a spectroscopic method that allows us to calibrate the rf electric field against the voltage setting of the utilized wave-form generator. With this method we compare experimental and calculated spectra of Rydberg atoms in the applied rf electric field. The readings obtained for the rf field are inherently calibration free because the atomic response to the field is invariable. The rich spectroscopic structure in the strong rf-mixing regime is critical in achieving the quoted 3% peak-to-peak calibration precision.

We have performed a three-dimensional numerical field calculation using ANSOFT MAXWELL software. The input parameters of the field calculation are the voltage setting of the rf signal generator, the measured distance between the rf field plates, the field-plate dimensions, and the geometry and the dielectric properties of the glass cell. The field calculation shows that dielectric shielding causes a minor rf-field reduction; the rf field the atoms experience is $\approx 92\%$ of the field without the glass cell. Comparing the calculated field value with the actual field value (obtained from the atom-based field measurement), we find that the actual field exceeds the calculated field by about 9%. The disagreement is small enough that it may be attributed to an impedance mismatch and possibly to mild rf resonances in the circuit. It must be stressed that the atom-based field measurement allows us to determine the rf field significantly better than the field calculation.

We also note that the experimental sample spectra shown Fig. 2 for fields $\geqslant 2.2$ V/cm exhibit somewhat larger linewidths than the calculated spectra (even after application of the convolution procedure explained in this section). The additional broadening may be due to strong, field-induced Rydberg-atom interactions (such as dipolar interaction between ac electric dipole moments). However, as already stated, additional studies will be required to develop a quantitative understanding of the broadening in high rf fields.

VI. PROSPECTS FOR RYDBERG-ATOM-BASED RF-FIELD MEASUREMENT

In order to exhibit the complexity of the Floquet spectra and to show how many quantum levels contribute to the experimentally observed spectra, in Fig. 5 we display the calculated relative excitation rates $S_{\nu,N}$ in the vicinity of one of the avoided crossings at several zoom levels at high resolution. The zoom levels are indicated by square boxes in Figs. 3(a) and 5 (left panel). In order to show the spectral details, in Fig. 5 we do not convolute the data; instead, the relative excitation rates $S_{\nu,N}$ are proportional to the symbol areas. Further, the exact positions of all levels are indicated by (equal-sized) crosses, regardless of excitation rate.

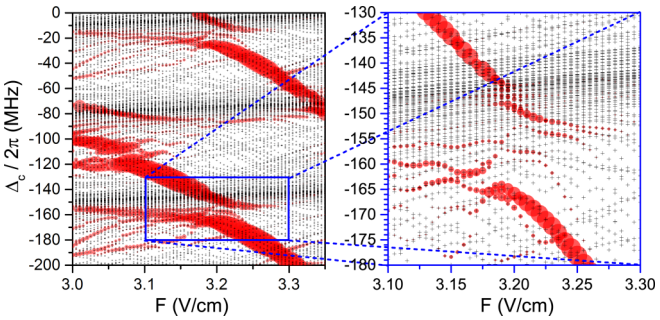

FIG. 5. Calculated relative excitation rates $S_{\nu,N}$ for the region denoted with a green square in Fig. 3(a) over the rf field ranges 3.0–3.33 V/cm (left) and 3.1–3.3 V/cm (right). The circle symbol areas are proportional to the relative excitation rates $S_{\nu,N}$.

Figure 5 demonstrates that the spectra and, in particular, the avoided crossings involve a large number of dressed atom-field Floquet states. Most of them remain undetected in the experiment because of their small excitation rates. Also, in the present experiment most levels that do have large excitation rates are not individually resolved. Using smaller spectroscopic cells, which have smaller rf-field inhomogeneity, and lower probe-laser power, translating into less saturation broadening as well as a reduced likelihood of line broadening due to Rydberg-Rydberg interactions, we expect to be able to resolve fine features such as the ones seen in Fig. 5. Higher spectral resolution will result in reduced uncertainty in calibration-free rf-field measurement. Inspecting the fine anticrossing structures in Fig. 5, we anticipate that absolute rf-field measurement with uncertainties in the range of 0.1% could be feasible.

VII. EFFECTS OF rf ANHARMONICITY AND dc OFFSET FIELDS

In an auxiliary study, we have also investigated modulation with a distorted rf signal that has a small degree of anharmonicity. The result of this measurement, also performed at a modulation frequency of 70 MHz, is shown in Fig. 6(a). In comparison with Fig. 3, where the applied rf modulation was a pure sine wave, the spectra in Fig. 6 exhibit additional anharmonicity-induced odd-order modulation bands, labeled with arrows. The odd sidebands apparently result from higher-harmonic components in the distorted harmonic rf field. To verify this assumption, we have computed numerous Floquet spectra for periodic rf fields with expansion $F(t) = F\,[\sum_{n=0}^{3}\alpha_n \cos(n\omega_m t) + \sum_{m=1}^{3}\beta_m \sin(m\omega_m t)]$. We set $\alpha_1 = 1$ to represent the main rf term and keep all other Fourier coefficients small. In view of earlier work [4] and Fig. 7, we expect that higher harmonics rather than the dc component of the distorted rf signal will give rise to the additional sidebands. In the modeling we have therefore focused on cases with $\alpha_0 = 0$ (which have a zero cycle-averaged field). In Fig. 6(b) we show a calculated Floquet spectrum for $\alpha_2 = 0.025$, with the symbol area proportional to $S_{\nu,N}$. In both experiment and calculation, the anharmonicity-induced odd-order modulation sidebands begin to emerge at about 2.5 V/cm and then quickly rise in visibility. At the high-field limit in Fig. 6, odd and even sidebands have similar visibility. Figure 6 and similar calculations demonstrate that rf modulation spectroscopy of Rydberg atoms is quite sensitive to anharmonic content in periodic rf wave forms and that the susceptibility of the atomic response to the anharmonicity increases with the rf field.

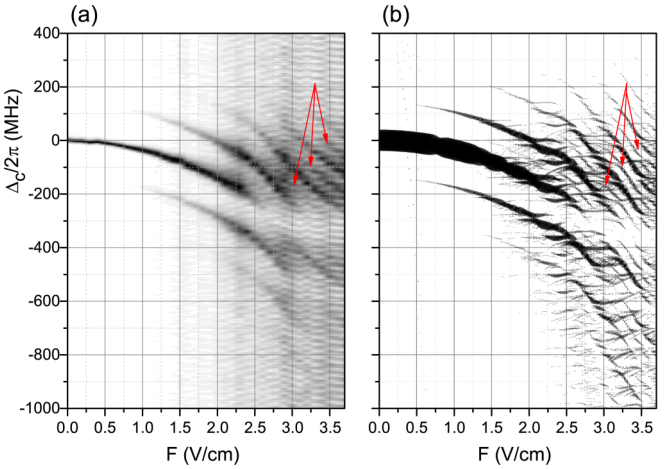

FIG. 6. Measurements and calculations similar to those in Fig. 3, but using a slightly anharmonic wave form. To enhance the signal at high rf field, the probe Rabi frequency for (a) has been chosen to be 1.5 times as large as in Fig. 3. The calculation in (b) is for an rf field $F_{RF}(t) = F[\cos(\omega_m t) + 0.025\cos(2\omega_m t)]$, with $\omega_m = 2\pi \times 70$ MHz. The symbol area is proportional to the relative excitation rates $S_{\nu,N}$.

Finally, we have analyzed the effect of a dc offset field on Floquet maps of the rf-modulated $57S_{1/2}$ Rydberg state. The directions of the applied dc and rf electric fields are parallel to each other, as evident from Fig. 1. In the calculation shown in Fig. 7(b), over the range of $F_{\rm DC}$ from 0 to 0.2 V/cm we

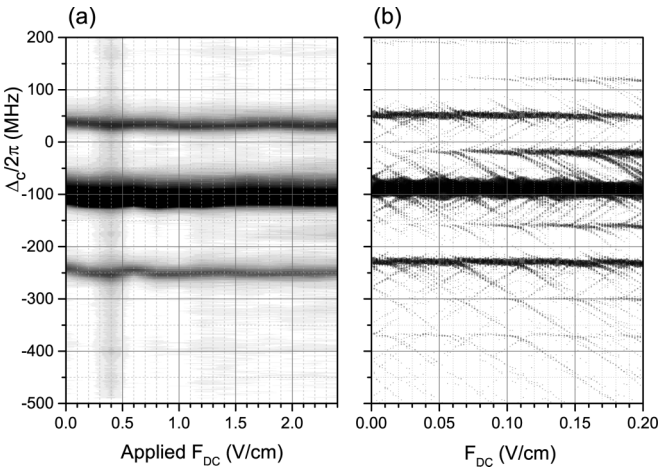

FIG. 7. (a) Experimental and (b) calculated Rydberg EIT spectra as a function of a dc offset field $F_{\rm DC}$ added to a purely harmonic rf modulation with frequency $\omega_m = 2\pi \times 70$ MHz and fixed amplitude $F = 1.6$ V/cm. In (a) the x axis shows the applied dc field, which is much larger than the shielded remaining dc field within the atom-field interaction region. To enhance sensitivity for weak odd-band signals, the probe Rabi frequency has been chosen to be 1.5 times as large as in Fig. 3.

see the strength of the first-order ($N = \pm 1$) sidebands rise to about 10% of the strength of the $N = 0$ band, in qualitative agreement with the low-field model in [21]. The dc Stark shift $-\alpha F_{\mathrm{DC}}^2/2$ is very minor and nearly invisible in Fig. 7(b). We also do not see any first-order sidebands in the experimental Floquet map shown in Fig. 7(a). The fact that an applied dc electric field is not effective in generating any visible atomic response can be attributed to a dc shielding effect, in which the dc electric field is screened by surface charges on the inside cell walls. The shielding effect, which has been reported before in Ref. [4], is attributed to ions and electrons produced by ionization of Rydberg atoms and the photoelectric effect on the cell walls. In the presence of an additional rf field (our case), the shielding effect persists, showing that the high-frequency field does not impede the dc shielding. From Fig. 7 we find a lower bound of the dc shielding factor of $\sim$100, limited by experimental sensitivity and the low value of the applied dc field. The actual shielding factor may be much higher.

VIII. CONCLUSION

In summary, we have studied rf-modulated Rydberg EIT spectra in a cascade three-level system in a cesium room-temperature vapor cell. The method allows for fast, all-optical readout of the rf-modified Rydberg level structure. The observed Rydberg Floquet spectra exhibit field-induced level shifts and sidebands in weak rf fields, whereas higher-order sidebands, complex state mixing, and level crossings with hydrogenic states are found in strong rf fields. Weak anharmonicity of the rf signal has been found to produce odd modulation sidebands. In work not shown we have obtained qualitatively similar results for modulation frequencies in the range from 40 to 80 MHz. The experimental results are well explained by our Floquet model, even considering details of the complex high-field spectra. The Rydberg EIT spectroscopy presented here could be applied in an atom-based technique for calibration of rf transmission systems and antenna-free measurement of rf electric fields. Future work may shed light on the observed increase of the spectral linewidth as a function of rf-field strength. Moderate improvements in the setup, such as smaller cells and lower probe power, are expected to enable more precise rf-field measurement.

ACKNOWLEDGMENTS

This work was supported by the State Key Development Program for Basic Research of China (Grant No. 2012CB921603), the Changjiang Scholars and Innovative Research Team in the University of the Ministry of Education of China (Grant No. IRT13076), the State Key Program of the National Natural Science of China (Grant No. 11434007), NNSF of China (Grants No. 11274209, No. 61475090), and a research project supported by the Shanxi Scholarship Council of China (2014-009). G.R. acknowledges support from the NSF (Grant No. PHY-1506093) and the BAIREN plan of Shanxi province.

[1] I. M. Savukov, S. J. Seltzer, M. V. Romalis, and K. L. Sauer, Phys. Rev. Lett. **95**, 063004 (2005).
[2] B. Patton, O. O. Versolato, D. C. Hovde, E. Corsini, J. M. Higbie, and D. Budker, Appl. Phys. Lett. **101**, 083502 (2012).
[3] T. F. Gallagher, *Rydberg Atoms* (Cambridge University Press, Cambridge, 1994).
[4] A. K. Mohapatra, T. R. Jackson, and C. S. Adams, Phys. Rev. Lett. **98**, 113003 (2007).
[5] A. K. Mohapatra, M. G. Bason, B. Butscher, K. J. Weatherill, and C. S. Adams, Nat. Phys. **4**, 890 (2008).
[6] C. Holloway, J. Gordon, S. Jefferts, A. Schwarzkopf, D. Anderson, S. Miller, N. Thaicharoen, and G. Raithel, IEEE Trans. Antennas Propag. **62**, 6169 (2014).
[7] J. A. Sedlacek, A. Schwettmann, H. Kübler, R. Löw, T. Pfau, and J. P. Shaffer, Nat. Phys. **8**, 819 (2012).
[8] H. Fan, S. Kumar, J. Sedlacek, H. Kübler, S. Karimkashi, and J. P. Shaffer, J. Phys. B **48**, 202001 (2015).
[9] J. A. Sedlacek, A. Schwettmann, H. Kübler, and J. P. Shaffer, Phys. Rev. Lett. **111**, 063001 (2013).
[10] J. A. Gordon, C. L. Holloway, A. Schwarzkopf, D. A. Anderson, S. Miller, N. Thaicharoen, and G. Raithel, Appl. Phys. Lett. **105**, 024104 (2014).
[11] D. Barredo, H. Kübler, R. Daschner, R. Löw, and T. Pfau, Phys. Rev. Lett. **110**, 123002 (2013).
[12] J. Grimmel, M. Mack, F. Karlewski, F. Jessen, M. Reinschmidt, N. Sándor, and J. Fortágh, New J. Phys. **17**, 053005 (2015).
[13] D. Budker and M. Romalis, Nat. Phys. **3**, 227 (2007).
[14] H. Q. Fan, S. Kumar, R. Daschner, H. Kübler, and J. P. Shaffer, Opt. Lett. **39**, 3030 (2014).
[15] C. L. Holloway, J. A. Gordon, A. Schwarzkopf, D. A. Anderson, S. A. Miller, N. Thaicharoen, and G. Raithel, Appl. Phys. Lett. **104**, 244102 (2014).
[16] H. Q. Fan, S. Kumar, J. Sheng, J. P. Shaffer, C. L. Holloway, and J. A. Gordon, Phys. Rev. Appl. **4**, 044015 (2015).
[17] C. Affolderbach, G. X. Du, T. Bandi, A. Horsley, P. Treutlein, and G. Mileti, IEEE Trans. Instrum. Meas. **64**, 3629 (2015).
[18] P. Böhi and P. Treutlein, Appl. Phys. Lett. **101**, 181107 (2012).
[19] A. Horsley, G. X. Du, M. Pellaton, C. Affolderbach, G. Mileti, and P. Treutlein, Phys. Rev. A **88**, 063407 (2013).
[20] A. Horsley, G.-X. Du and P. Treutlein, New J. Phys. **17**, 112002 (2015).
[21] M. G. Bason, M. Tanasittikosol, A. Sargsyan, A. K. Mohapatra, D. Sarkisyan, R. M. Potvliege, and C. S. Adams, New J. Phys. **12**, 065015 (2010).
[22] S. Yoshida, C. O. Reinhold, J. Burgdörfer, S. Ye, and F. B. Dunning, Phys. Rev. A **86**, 043415 (2012).
[23] Y. Zhang, M. Ciocca, L.-W. He, C. E. Burkhardt, and J. J. Leventhal, Phys. Rev. A **50**, 4608 (1994).
[24] D. A. Anderson, A. Schwarzkopf, S. A. Miller, N. Thaicharoen, G. Raithel, J. A. Gordon, and C. L. Holloway, Phys. Rev. A **90**, 043419 (2014).
[25] D. A. Anderson, S. A. Miller, G. Raithel, J. A. Gordon, M. L. Butler, and C. L. Holloway, Phys. Rev. Appl. **5**, 034003 (2016).
[26] A. Reinhard, T. C. Liebisch, B. Knuffman, and G. Raithel, Phys. Rev. A **75**, 032712 (2007).